Prediction and Quantification of Micromixing Intensities in Laminar Flows

S. Cerbelli, M. M. Alvarez, and F. J. Muzzio
Dept. of Chemical and Biochemical Engineering, Rutgers University, Piscataway, NJ 08855

A new approach presented here predicts and quantifies the nonuniform spatial distribution of passive interfaces in both periodic and aperiodic chaotic mixing processes. Based on a coarse-grained calculation of line element stretching, it bypasses the direct numerical simulation of continuous interfaces, which is computationally impractical even in simple model flows. The evolution of the structures created by the Lagrangian displacement and deformation process is decoupled into the product of a time-invariant, spatially-dependent function expressing the nonuniform density of interface throughout the flow domain and a temporally-dependent function expressing the exponential growth of the interface, characterized by a global exponent (topological entropy) unambiguously different from the Lyapunov exponent. The Sine Flow agreed excellently with the Journal Bearing, when results from direct tracking of the interface were compared to those using stretching calculations to predict interface density.

Introduction

The yield and product distribution of many manufacturing processes that involve multiple simultaneous chemical reactions can depend heavily on the efficiency of mechanical (convective) mixing. Convection causes displacement, and stretching and folding of fluid volumes. This results in segregated regions into close contact, causing an overall reduction of the characteristic length of segregation, and, consequently, more intense concentration gradients. In most processes, turbulence is used to achieve efficient fluid mixing for low viscosity materials. Efficient mixing of highly viscous systems, on the other hand, remains an open problem.

Aref (1984) showed that deceptively simple chaotic flow fields can promote efficient mixing in the absence of turbulence. This observation motivated extensive study of convective mixing in laminar chaotic flows by direct analytical, computational, and experimental methods. (A comprehensive introduction to the subject is given in Ottino (1989), and more recent advances can be found in Fountain et al. (1998), Hobbs et al. (1997) and other cited literature.) To date, however, we lack the means to measure or predict even the most basic attributes of the mixing microstructure, either in turbulent or laminar flows.

Parallel to these studies, the analysis of simplified one-dimensional (1-D) (lamellar) models of stirred systems undergoing simultaneous diffusion and reaction demonstrated that the product yield is strongly influenced by the geometric properties of the mixing structures resulting from mechanical agitation (Sokolov and Blumen, 1993; Muzzio and Ottino, 1989). (These models are based on the experimental observation that the partially-mixed structures generated by convection are spatially organized in an alternating pattern of striations (*lamellae*) that are nearly parallel to each other within most of the flow domain.)

As an illustration, consider a "thought experiment" in a 2-D flow where a subregion of the flow domain, marked with a gray tracer (Figure 1a), is being mechanically mixed with the surrounding fluid (white) by the effect of a flow field $\boldsymbol{v}(\boldsymbol{x}, t)$ (Figure 1b). In the diffusionless limit, the lamellae are determined by the intersections of the Intermaterial Contact Area (ICA), also referred to as the Interfacial Area (shown as a black solid line in the figure), with a generic sampling path (the dashed line). Since the lamellae size distribution controls diffusion and reaction in the system, even at the most simplified level of investigation, the ability to assess the influence of convection on the dynamics of diffusing-reacting mixtures relies upon the knowledge of the geometric features of ICA.

Correspondence concerning this article should be addressed to F. J. Muzzio.

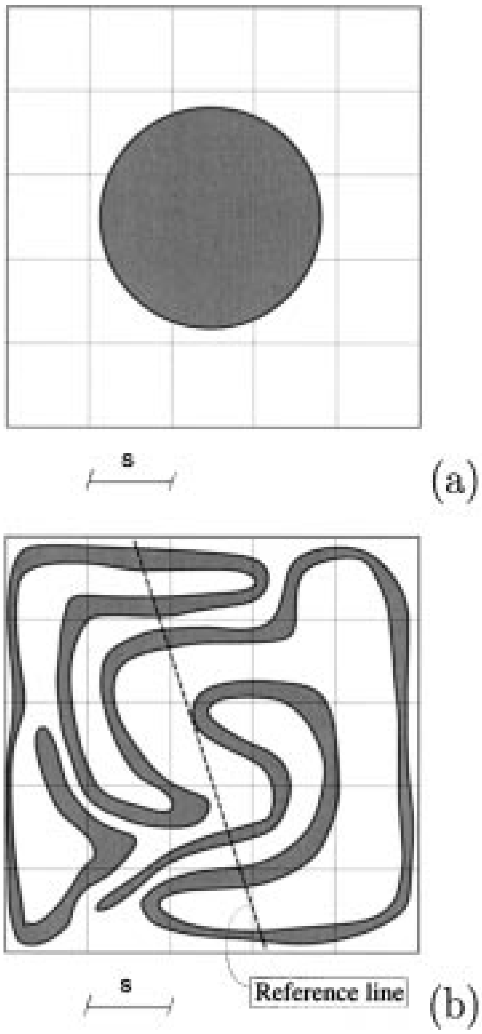

Figure 1. Mixing due to convection.

From the point of view of reaction engineering, optimal yield and control usually require that the ICA be generated as *quickly* and as *uniformly* as possible, in order to minimize departure from the "perfect mixedness" hypothesis of the CSTR model.

Recently, a new approach for the study of ICA dynamics has been developed in the context of 2-D time-periodic chaotic flows (Muzzio et al., 2000, Giona et al., 1999, Cerbelli et al., 2000). By studying the system in a stroboscopic time-frame (that is, where snapshots are taken at multiples of the periodicity interval), it was shown that the Asymptotic Directionality (AD) property can be used to explain the spatial organization of material lines as they are passively convected and deformed by the flow field. In short, AD is the property by which any material line embedded in the chaotic region converges towards a space-filling *time-invariant* structure, regardless of its initial location, size, or shape. Furthermore, the local spatial density of ICA is also time-invariant and *permanently* nonuniform (Muzzio et al., 2000; Giona et al., 1999). More precisely, by subdividing the flow domain in N_c cells of size δa, the local density $\langle \rho \rangle_{x_i}$ at the center of each cell is defined as the fraction L_i of the total interface length

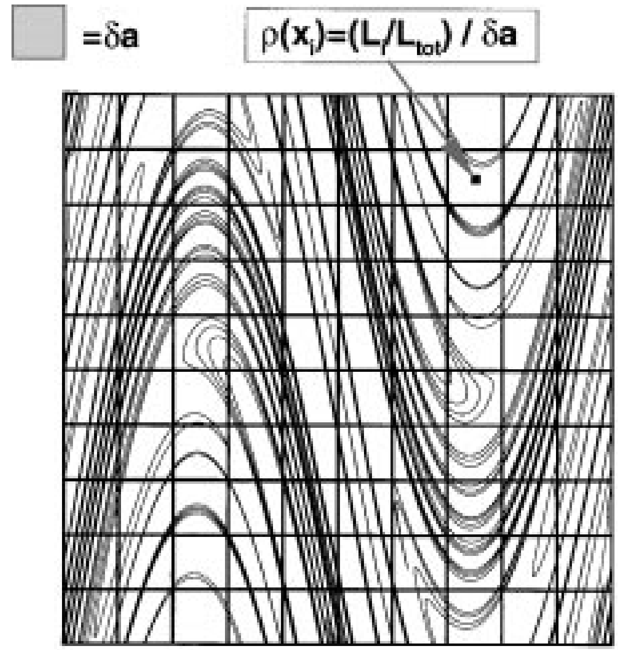

Figure 2. Definition of the coarse-grained density of ICA.

The flow domain is divided in N_b cells, and the box density $\langle \rho \rangle_{x_i}$ at the cell mid-point $\boldsymbol{x}_i$ is computed as the fraction of the filament length that falls within the cell, divided by the cell-area δa.

L_{Tot} that falls within the cell centered at $\boldsymbol{x}_i$, divided by the cell area δa (Figure 2). One can anticipate one of the main results presented in this article. As a result of the invariance of ICA structure and dynamics, after a (very brief) transient, the amount of interface length L_i falling within the box centered at $\boldsymbol{x}_i$ follows the relation

$$L_i = L_{0i} \langle \rho \rangle_{x_i} e^{\nu t} \delta a \tag{1}$$

where L_{0i} is the initial amount of interface in the box i, $\langle \rho \rangle_{x_i}$ *is only a function of position*, t is time, and ν is a global exponent known as topological entropy. In other words, Eq. 1 decouples the spatio-temporal mixing dynamics into the product of a time-independent function $\langle \rho \rangle_{x_i}$ which captures the spatial modulation, multiplied by the overall exponential stretching of the interface length expressed by the term $e^{\nu t}$. *Since the interface grows everywhere at the same rate, and since most quantities of interest (for example, the diffusional length scale) can be defined from* $\langle \rho \rangle_{x_i}$, the exponent ν is the true characteristic rate of the mixing process.

The importance of this finding can be readily understood when considering that should Eq. 1 be confirmed as a generic property of efficient mixing devices, it would allow the inherently Lagrangian analysis of reaction dynamics to recast into a Eulerian form, where one can approximate the reactor as an array of cells, each characterized by its own local degree of micromixing $\langle \rho \rangle_{x_i}$.

From a practical point of view, the major obstacle in quantitatively pursuing this approach is the inability to describe the complicated, nested-heterogeneous structure resulting from the mixing process. More precisely, due to the increasingly nonuniform stretching experienced by fluid elements, computation of the interface structure requires the convected coordinates of an exponentially increasing number of interface points. (Details are given in the "Tracking of material interfaces" section.) These computation difficulties make it impractical to implement tracking algorithms, even for the simplest real-world flows. Hence, alternative approaches are needed.

The objectives of this article are to: (1) Analyze the AD property and, in particular, the validity of Eq. 1 in the general context of 2-D time-dependent flows, both periodic and aperiodic; and, (2) Define an alternative method for computing the density of ICA that is feasible for realistic industrial-relevant flow situations.

First, we introduce the flow systems, and provide some background on local Lagrangian analysis. Tracking algorithms are also discussed. Next, the analysis of finite-sized interface dynamics is undertaken in the context of time-periodic flows. Third, focus on the connection between the local line-element stretching and the global process of interface generation is discussed, and the relationship needed to predict ICA density from local stretching averages is derived. The case of aperiodic flows is analyzed and the concept of stationary ICA density is generalized for this broader framework. Last, conclusions and a discussion regarding the relevance of the results for industrial mixing systems are presented.

Flow Systems and Kinematic Approach

In this section, we briefly discuss the relevant theoretical background using 2-D chaotic flow examples: the Sine Flow (SF), and the Journal Bearing (JB) systems.

A simplified model for laminar mixing flows: The Sine-Flow system

The SF (Alvarez et al., 1998) is a nonlinear model flow representative of the behavior of real systems, while also computationally inexpensive. This model is a piecewise continuous time-dependent flow $\boldsymbol{v}(\boldsymbol{x},t)$ obtained by alternately applying two steady sinusoidal velocity profiles $\boldsymbol{v}_1(\boldsymbol{x}) = [\sin(2\pi x), 0]$, $\boldsymbol{v}_2(\boldsymbol{x}) = [0, \sin(2\pi y)]$ orthogonal to each other, to the unit square box I^2 equipped with periodic boundary conditions (Figure 3). In other words, whenever a fluid particle crosses one of the boundaries, it is assumed to instantaneously reenter the unit box through the opposite side. Since $\boldsymbol{v}_1$ and $\boldsymbol{v}_2$ each only depend on one of the two spatial coordinates, the trajectories of the the fluid point particles are piecewise straight lines. Once the duration τ of each motion has been defined, the ODE system expressing the purely convective motion

$$\dot{\boldsymbol{x}} = \boldsymbol{v}(\boldsymbol{x}, t) \tag{2}$$

can be integrated by inspection yielding

$$\Phi_\tau(\boldsymbol{X}) = \boldsymbol{X} + \int_0^\tau \boldsymbol{v}_i(\boldsymbol{X})dt = \boldsymbol{X} + \boldsymbol{v}_i(\boldsymbol{X})\tau \quad (\text{mod. } 1) \tag{3}$$

where Φ_τ is the map that brings the generic point located at $\boldsymbol{X}$ into the new position $x = \Phi_\tau(X)$ after the elapsed time τ.

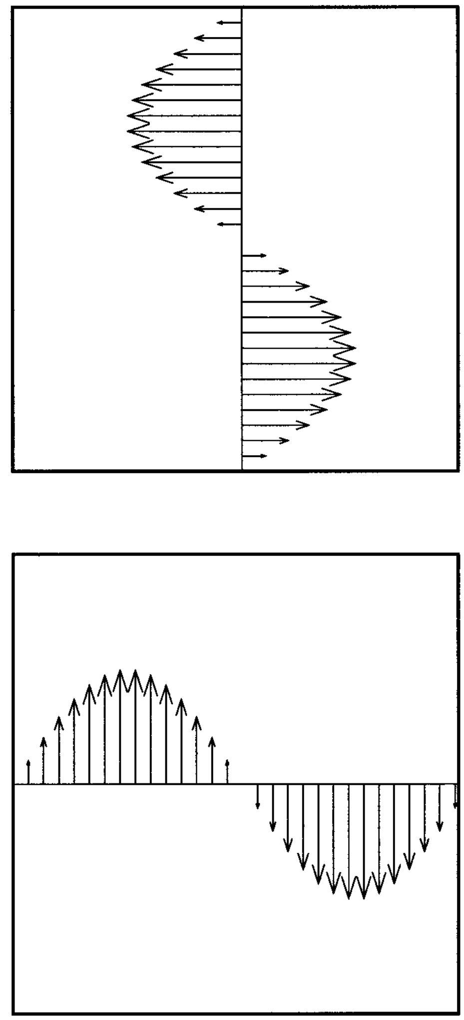

Figure 3. Two sinusoidal velocity profiles; top $v_1(x)$, bottom $v_2(x)$, defining the SF system in the " unfolded" representation of the flow domain.

Whenever a fluid particle crosses one of the boundaries, it is assumed to instantly re-enter the unit box on the opposite side.

Periodic and aperiodic recipes are defined by a sequence of intervals $\{\tau_1, \tau_2, \ldots \tau_n, \ldots\}$, where the velocity fields act alternately for the time intervals specified by the sequence. The case of a periodic recipe is thus specified by a sequence where all the time intervals are equal, $\tau_i = T/2$, where T is the overall period of the flow field. The dynamics at multiple integers of the period are then specified by the repeated application of the Poincaré map, which is obtained by composition of the two motions along the two half-periods τ. The *aperiodic* recipes considered in this article are generated as a perturbation of a given periodic case (period $T = 2\tau$) according to the scheme

$$\tau_i = (1 + \alpha\beta_i)\tau \tag{4}$$

where β_i is a random variable uniformly distributed in the interval $[-1; 1]$, $\alpha < 1$ is a positive constant yielding the strength of the perturbation, and $\tau = \langle T \rangle/2$ is the nominal (average) period along which each motion is acting.

The availability of a piecewise closed-form solution for the motion in the SF system makes this model suitable for highly accurate and relatively inexpensive computer simulations, where the only source of error is round-off. Although the sinusoidal profile does not belong to the class of solutions of Navier-Stokes equations, the SF model has been proven to share most of the dynamic features characteristic of real mixing systems (Hobbs et al., 1997).

Journal Bearing system

The Journal Bearing system is a 2-D flow defined in the region between eccentric cylinders, and is generated by alternately rotating inner and outer cylinders. The geometry of the system is specified by two dimensionless parameters, namely the radius ratio $r = R_{out}/R_{inn}$, and the eccentricity $\epsilon = e_c/R_{inn}$, where e_c is the distance between the centers of the inner and outer circles (Figure 4). The JB flow has been the object of intense investigation over the past 15 years (Ottino, 1989), mainly because an analytical solution for the creeping flow regime is available (Wannier, 1950), making it possible to pursue a kinematic characterization (Poincaré sections, stretching distributions) with good accuracy. In the remainder of this work, it is assumed that $r = 3$ and $\epsilon = 0.225$. We analyze the mixing dynamics for protocols where the inner and outer cylinders are alternately co-rotating. The aperiodic recipes are generated according to Eq. 4.

Kinematics of time-periodic flows

As mentioned in the Introduction, the idea that a laminar flow can generate efficient convective mixing was introduced by Aref (1984). He first recognized the Hamiltonian structure of the equations expressing the passive convection of a fluid particle in incompressible 2-D flows. Since then, a number of experimental and computational works on the subject made it evident that the problem of assessing mixing performance begins, rather than ends, with the specification of the flow field $\boldsymbol{v}(\boldsymbol{x}, t)$. In general, a simple functional form for $\boldsymbol{v}$ does not imply a simple functional form for the integral trajectories of the system $\dot{\boldsymbol{x}} = \boldsymbol{v}(\boldsymbol{x},t)$. As far as mixing applications are concerned, it turns out that the most important case is precisely the one for which most of the fluid particles follow chaotic motion, which brings them to visit with equal probability any given location of a massive subregion (chaotic region) of the flow domain.

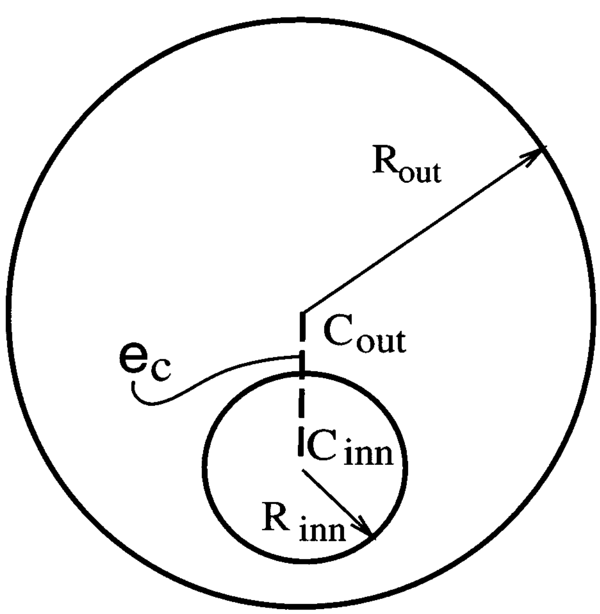

Figure 4. Geometric parameters for the JB system.

Chaos and islands

In cases where flow is time-periodic, the Poincaré sections technique is commonly used to determine the size of chaotic and nonchaotic regions. The Poincaré section is simply the superposition onto a single plot of all the locations visited by a generic fluid particle at times that are multiple of the flow period. Figure 5a shows the result of this computation for seven initial conditions for the periodic protocol $T = 0.4$ in the SF system. For this value of T, most of the trajectories (shown in Figure 5a as initial conditions A through F) are constrained onto 1-D loops (KAM curves), which enclose poorly mixed regions (islands). Material enclosed in an island is thereafter confined for all times. Mixing within the islands, if any, is driven only by diffusion—typically a very slow process. Conversely, the initial condition F appears to uniformly fill a 2-D x-shaped region. Any other particle in this region would generate the same outcome. The above landscape can change dramatically when the protocol is modified. In particular, the size of the islands can be progressively shrunk until an optimal mixing condition is reached where the chaotic region invades nearly all of the flow domain (Figure 5b).

In summary, the Poincaré sections analysis allows one to identify the presence and shape of massive segregated regions for any given periodic protocol, thus indicating the optimal protocol from a macromixing standpoint. However, Poincaré sections do not provide any information about the dynamics within the chaotic region itself. Indeed, in a nearly globally chaotic condition such as the one depicted in Figure 5, any chaotic orbit fills almost all of the flow domain densely and *uniformly* leading to the conclusion that chaotic dynamics in area-preserving systems is structureless and featureless. As will be presented in the remainder of this article, a well-defined geometric and dynamic structure emerges within the chaotic region as soon as the focus is shifted from massless point particles to continuous interfaces dynamics.

Stretching

The first step toward understanding ICA dynamics is the characterization of the evolution of an infinitesimal arc ds at a point $\boldsymbol{X}$ of a material line Γ undergoing displacement and deformation by the action of the velocity field $\boldsymbol{v}(\boldsymbol{x}, t)$. Within a linear approximation, the line element ds can be viewed as a vector $\delta \boldsymbol{X}$ applied at $\boldsymbol{X}$. In the discrete framework, the dynamics of $\delta \boldsymbol{X}$ is specified by the Jacobian matrix $\nabla \boldsymbol{\Phi}$ of spatial derivatives of the Poincaré map $\boldsymbol{I}$, meaning that the image $\delta_n \boldsymbol{x}$ of $\delta \boldsymbol{X}$ after n recursive applications of $\boldsymbol{\Phi}$ is given by

$$\delta_n \boldsymbol{x} = \delta \boldsymbol{X} \cdot \nabla \boldsymbol{\Phi}^n |_{\boldsymbol{x}} \tag{5}$$

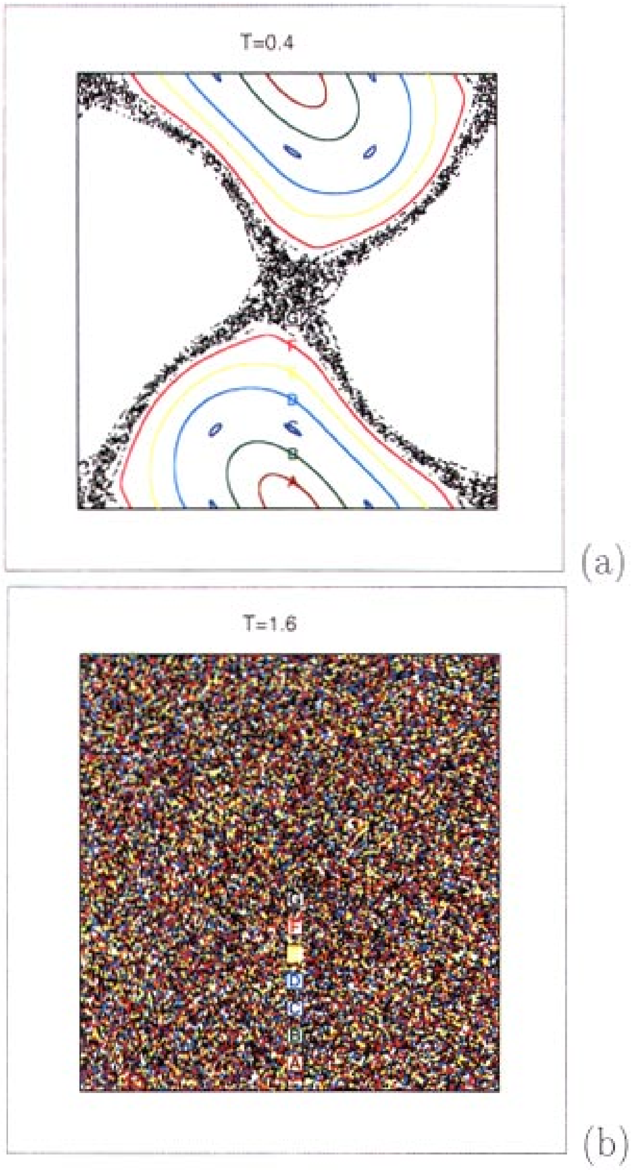

Figure 5. Poincaré sections of seven initial conditions (labeled A through G) for the SF map with (a) $T = 0.4$ and (b) $T = 1.6$.

The image vector $\delta_n \boldsymbol{x}$ is then a function of both the modulus and orientation of the vector $\delta \boldsymbol{X}$, and of the initial location $\boldsymbol{X}$ of $\delta \boldsymbol{X}$ within the flow domain. This latter dependence can be recognized in the Jacobian matrix $\nabla \boldsymbol{\Phi}^n|\boldsymbol{x}$ of the n-th order mapping $\boldsymbol{x}_n = \boldsymbol{\Phi}^n(\boldsymbol{X})$, which by the chain rule factorizes into the product of n Jacobian matrices $\nabla \boldsymbol{\Phi}$ of the one step map $\boldsymbol{\Phi}$, evaluated along the orbit of ds at $\boldsymbol{x}_0 = \boldsymbol{X}$, $\boldsymbol{x}_1 = \Phi(\boldsymbol{X}),\ \ldots,\ \boldsymbol{x}_{n-1} = \boldsymbol{\Phi}^{n-1}(\boldsymbol{X})$

$$\nabla \boldsymbol{\Phi}^n|_{\boldsymbol{x}} = \int_{i=0}^{i=n-1} \nabla \boldsymbol{\Phi}|_{\boldsymbol{x}_i} \tag{6}$$

The ratio

$$\lambda_n(\boldsymbol{X}, \boldsymbol{T}) = \frac{\| \delta_n \boldsymbol{x} \|}{\| \delta \boldsymbol{X} \|} \tag{7}$$

is called n-th period stretching factor relative to the point $\boldsymbol{X}$ and to the direction $\boldsymbol{T} = \delta \boldsymbol{X} / \| \delta \boldsymbol{X} \|$. By defining $\boldsymbol{t}_0 = \boldsymbol{T}$, $\boldsymbol{t}_i = \boldsymbol{t}_{i-1} \cdot \nabla \boldsymbol{\Phi}|_{\boldsymbol{x}_{i-1}} / \| \boldsymbol{t}_{i-1} \cdot \nabla \boldsymbol{\Phi}|_{\boldsymbol{x}_{i-1}} \|$ one obtains that the n-th order stretching factor can also be expressed as the product of the one-step stretching $\lambda_{i,i+1}$

$$\lambda_n(\boldsymbol{X}, \boldsymbol{T}) = \prod_{i=0}^{i=n-1} \lambda_{i,i+1} \tag{8}$$

Since $\nabla \boldsymbol{\Phi}$ is a function of position, the dynamics of one-step stretchings experienced by a generic vector is composed of a history of heterogeneous events as the vector visits different locations of the flow domain. The consequence of this phenomenon is that ICA spreads nonuniformly throughout the chaotic region.

Tracking material interfaces

A global representation of the convective mixing problem can be obtained by examining the evolution of a "macroscopic" (finite-sized) subregion A in Figure 5a of the flow domain undergoing deformation by the action of the flow field. We begin our study by considering the SF system. As a concrete example, the case for which A is a circle centered at $(x_c,\ y_c) = (1/2,\ 1/2)$ with radius $R = 1/2$ is considered throughout. Due to the aforementioned AD property that is characteristic of chaotic systems, any other initial condition would generate essentially the same result.

Numerical simulations of continuous material lines are relatively recent in the chaotic dynamics literature (Alvarez et al., 1998). The first problem to be faced is that at each point of the curve Γ that defines the boundary of A, stretching accumulates nonuniformly, and the difference between the minimum and maximum of stretching values experienced by the curve arcs increases with time. Thus, if one starts with a uniform array of points along the initial curve Γ, the images of such points through iterations of the Poincaré map are distributed heterogeneously along $\gamma_n = \Phi^n(\Gamma)$ (Figure 6). As a result, the structure of the material interface is rapidly lost.

A substantial improvement can be accomplished by interpolating points on the original curve Γ in such a way that the distance between two consecutive points on the image curve γ_n after n iterations of the Poincaré map does not exceed a certain threshold value, say $d_{\max}$ (Alvarez et al., 1998).

In this article, a refinement of this criterion is implemented in order to obtain a nearly uniform distribution of points along γ_n. The algorithm defining the initial distribution of points is based on the stretching experienced by a unit vector $\boldsymbol{T}$ tangent to Γ at a generic point $\boldsymbol{X} \in \Gamma$. More precisely, let $\boldsymbol{X}$, $\boldsymbol{Y}$ be two points on Γ separated by a distance Δ along the curve arc, and $\boldsymbol{T}$, be a unit vector tangent to Γ at $\boldsymbol{X}$. Let also $\boldsymbol{x}$, $\boldsymbol{y}$ be the images of $\boldsymbol{X}$, $\boldsymbol{Y}$ on $\gamma = \Phi^n(\Gamma)$, and δ the distance between $\boldsymbol{x}$, $\boldsymbol{y}$ along γ. If Δ is small enough, then a linear approximation for distances holds, and one can write

$$\frac{\delta}{\Delta} \sim \lambda_n(\boldsymbol{X}, \boldsymbol{T}) \qquad \Rightarrow \Delta = \frac{\delta}{\lambda_n(\boldsymbol{X}, \boldsymbol{T})} \tag{9}$$

Starting from an arbitrary point $\boldsymbol{X}_0 \in \Gamma$ and fixing a value for δ, the equation can be used to find the initial distribution of

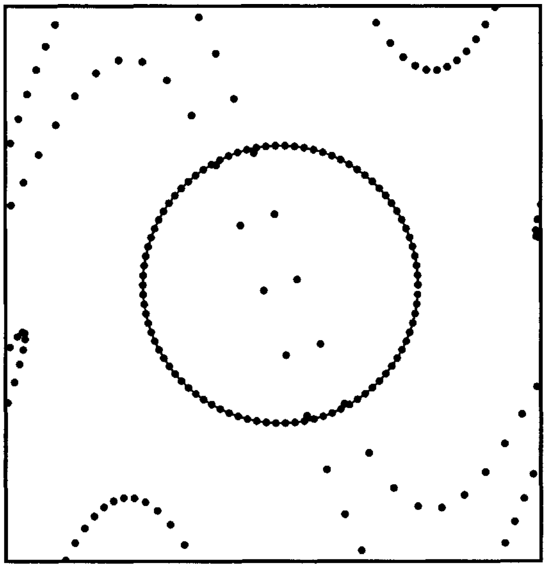

Figure 6. Numerical tracking of ICA.

If the initial curve Γ (circle) is represented by a uniform array of points, their images on the transformed curve γ are distributed unevenly at a later time because stretching at each point of Γ is nonuniform.

points along the initial curve that yields a nearly uniform distribution of points along the current curve γ. Figure 7 shows the nonuniform distribution of points on the original circle that generates a nearly uniform distribution of points along the transformed filament.

Indeed, as $\delta \to 0$, the distribution of distances along γ converges toward a Dirac's delta distribution centered at δ (not shown in the interest of brevity). However, the implementation of this algorithm for a chaotic flow requires considering an exponentially growing number of points as time increases. Furthermore, an accumulation of errors will then cause the criterion expressed by Eq. 9 to fail, meaning that, for any $\Delta > 0$, the actual distance d of the image points will not satisfy the relationship $d \approx \delta$. (Common sources of error are round-off, numerical integration of the flow field, and numerical determination of the flow field itself. In a real flow all of these errors are present at the same time.)

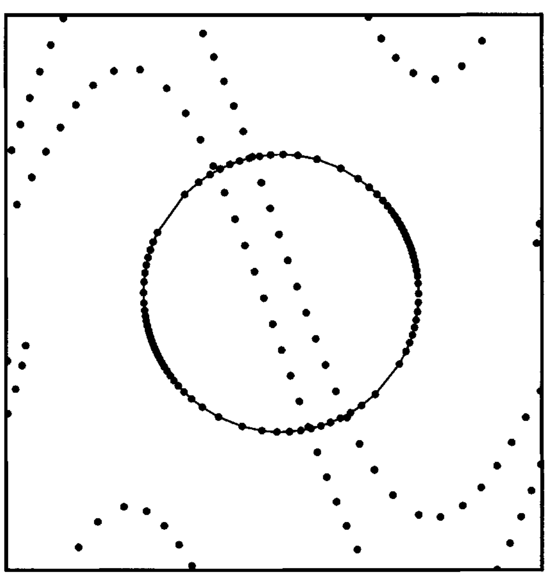

Figure 7. Tracking of ICA.

The nonuniform distribution of points along the circle, determined based on the stretching algorithm, yields a uniform covering of the convected filament.

Hence, direct tracking of interfaces in chaotic flows is not a realistic proposition, and it is necessary to define an alternative method to quantify the spatial distribution of ICA. This goal is undertaken is the following sections.

Micromixing Intensities and ICA Structure in Time-Periodic Flows

In this section, results of ICA tracking for the SF and JB systems are presented. For all cases considered, the original configuration of the filament was taken as a circle of size comparable to the linear dimensions of the flow domain.

The implementation of the stretching algorithm defined by Eq. 9 requires evaluating the n-th fold stretching value (Eq. 7) at each point of the curve Γ representing the filament at the initial time. If Γ is known through its parametric representation, its local unit tangent vector can be obtained by differentiation. Therefore, one is left with the determination of the Jacobian matrix $\nabla\Phi^n$ along the trajectory. Since the Poincaré map Φ is known analytically in the SF system, its spatial derivatives can also be obtained by direct differentiation. In all the cases presented below, the initial circle was taken centered at the point (1/2, 1/2) with radius $R_c = 1/2$ (Figure 7).

Figure 8 shows the structure of the filament for $n = 1, 2, 3, 4$ periods with $T = 1.6$ (nearly global chaos; compare with the Poincaré section in Figure 5). Several qualitative observations can be made:

(1) The filament rapidly converges toward a curved structure that invades the chaotic region.

(2) The local orientation of the curve attains time-independent behavior. The structure displays an ever-increasing degree of detail from one period to the next, but its topological features remain unchanged.

(3) The space-filling dynamics of the filament is *nonuniform*, meaning that in some regions of the flow domain ICA is packed "more densely" than in others. This feature is not transient.

It is important to point out that the geometric properties of the chaotic region revealed by material line dynamics are "invisible" to the conventional analysis of Poincaré sections of discrete points. As shown in Figure 5, the plot of single particles trajectory appears as a featureless cloud of points uniformly distributed within the chaotic region. The same qualitative features can be observed in the JB system. Figure 9 shows the evolved structures for the first four periods of a circle of the same diameter as the inner cylinder initially symmetrically placed in the gap between the two cylinders. The globally chaotic protocol is obtained in this case by alternately co-rotating the outer and the inner cylinders through the angles $\theta_{out} = 2\pi$, and $\theta_{inn} = 3\theta_{out}$.

The first quantitative parameter describing ICA dynamics is the overall growth rate of the interface vs. time. Figure 10

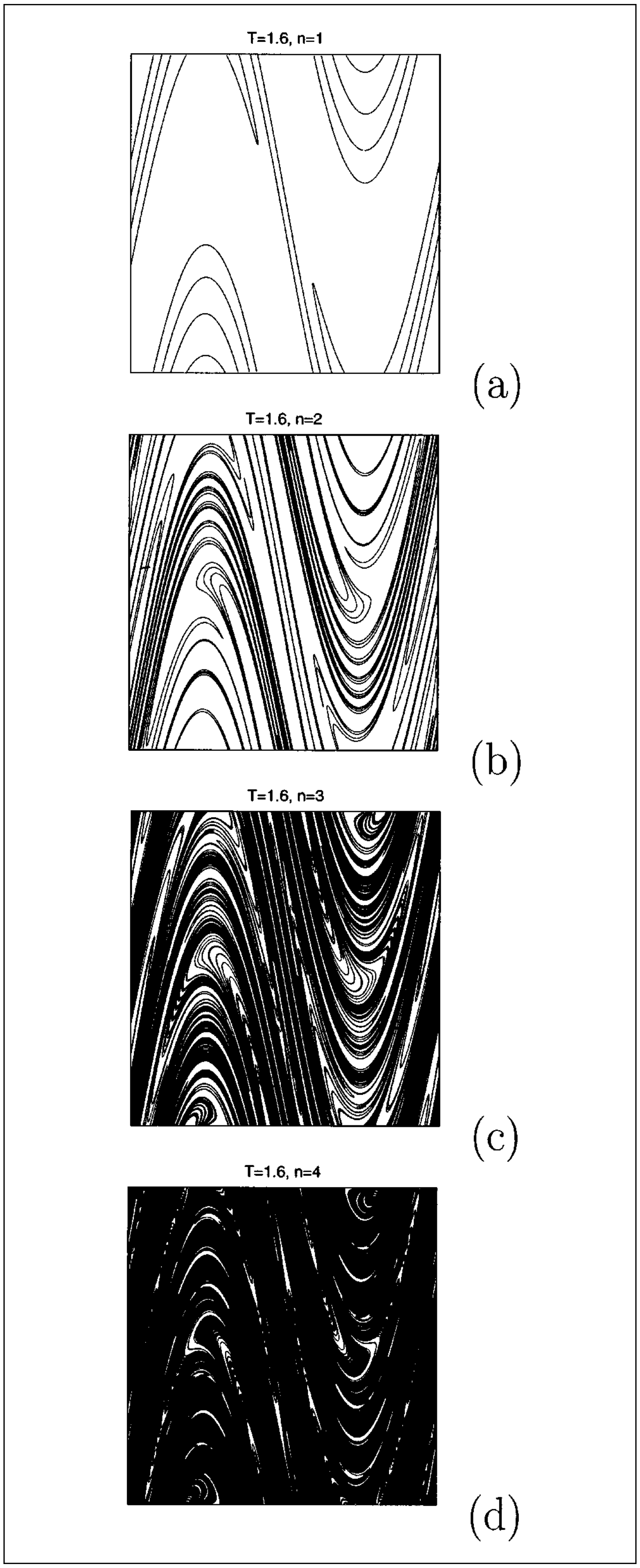

Figure 8. ICA dynamics in the SF system under the periodic protocol $T = 1.6$.

Frames represent the evolved structure of a circle of radius $R = 1/2$ with center at the midpoint of the unit box after $n = 1, 2, 3, 4$ iteration of the Poincaré map. The overall filament structure appears to be *time invariant*.

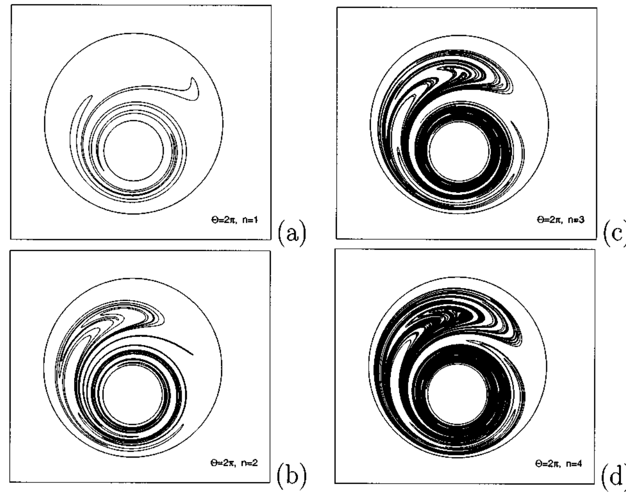

Figure 9. ICA dynamics in the JB system for the protocol defined by $\theta_{out} = 2\pi$.

The initial condition was a circle of the same size of the inner cylinder with center located on the axis of symmetry (y-axis) at half distance from the walls.

reports the logarithm of the length ratio L_n/L_0 for the periodic protocols $T = 0.4$, 0.8, 1.6, in the SF. In all cases the rate of growth displays exponential behavior. The slope of the straight lines is the so-called topological entropy (Newhouse, 1986; Katok and Hasselblatt, 1995), which we denote by ν. The exponent ν is strictly greater than the Lyapunov exponent Λ (Alvarez et al., 1998). From a theoretical standpoint, one can generally prove $\mu \geq \Lambda$ (Katok and Hasselblatt, 1995). The global analysis of length growth does not take into account differences in the spatial distribution of ICA.

In order to quantify this critical aspect of the mixing structure, a coarse-grained calculation of box densities $\langle \rho^{(n)} \rangle_{x_i}$ is carried out, as described in the Introduction, by subdividing the unit square into $N_c = 150 \times 150$ cells and computing, at

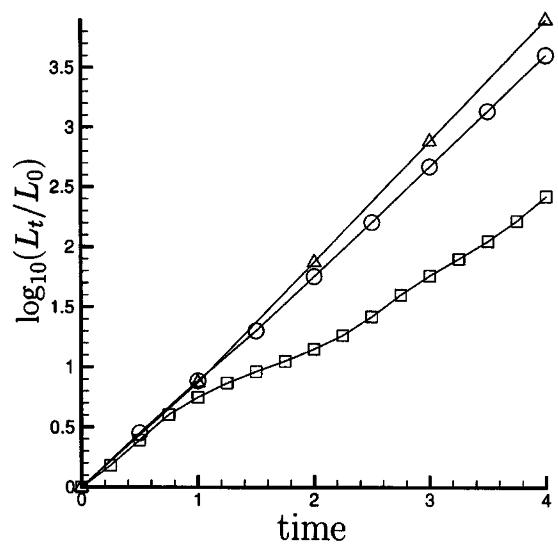

Figure 10. Rate of growth of ICA in the SF system.

Triangles: $T = 1.6$; circles: $T = 0.8$; squares: $T = 0.4$.

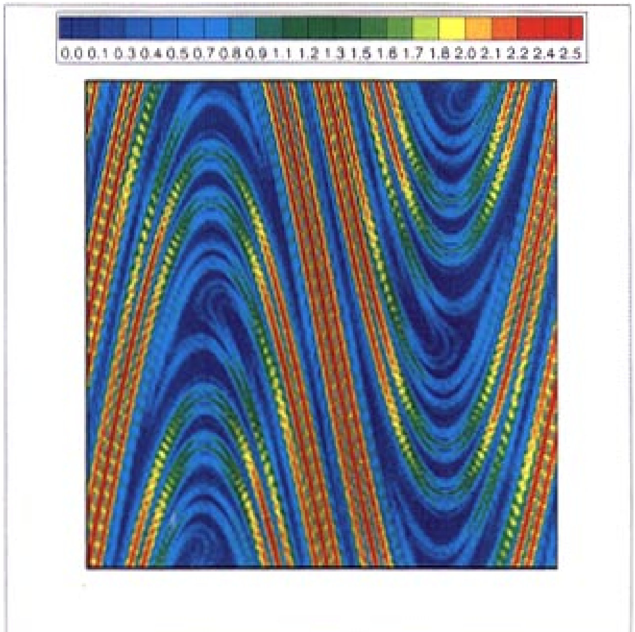

Figure 11. Color-contour plot of the ICA box-counted density for the filament reported in Figure 8d ($T = 1.6$, $n = 4$ periods).

The unit square I^2 was subdivided in 150×150 square boxes. The density at the center of each box was calculated as the fraction of filament length that falls within that box.

each time n, the fraction of the filament length that falls within each cell. The contour plot of the function $\langle \rho^{(n)} \rangle_{x_i}$, where x_i represents the center of each cell i, is shown in Figure 11 for the SF system, $n = 4$ and $T = 1.6$. The spatial behavior of $\langle \rho^{(n)} \rangle_{x_i}$, as well as its range of variability ($\rho_{\min}$, $\rho_{\max}$), is clearly dependent on the type of coarse-graining chosen to discretize the flow domain. However, *for a fixed mesh size*, the function $\langle \rho^{(n)} \rangle_{x_i}$ becomes *independent of time*. With the aforementioned choice for the mesh, the range of variability of $\langle \rho^{(n)} \rangle_{x_i}$ obtained spans the interval (0.01, 4). This means that, at this spatial scale of investigation, some boxes contain 400 times more interface than others. The highest values are found in the box located at the center (1/2, 1/2), which contains a hyperbolic fixed point for the Poincaré map Φ. The time-invariance of the density is made evident by computing probability density function (PDF) $F(\rho)$, that is, the frequency of occurrence of values of ρ_i. This last function is constructed by dividing the interval ($\rho_{\min}$, $\rho_{\max}$) in N_b cells, and assigning to the midpoint of each cell a value F equal to the fraction of values ρ_i that fall within that cell. Figure 12 shows the plot of $F(\rho^{(n)})$ for $n = 3, 4$ for the case $T = 1.6$. The convergence toward an invariant distribution is reached in this case after just three iterations of the Poincaré map.

The same features of ICA dynamics can be observed in the JB system, both at the global and local scales. In particular, the ratio L_n/L_0 vs. time (not shown in the interest of brevity) confirms that the length growth rapidly acquires exponential behavior. The density contour plot for the case $\theta_{out} = 2\pi$ is reported in Figure 13 (compare with the ICA structures of Figure 9). The high density region in this case is located in the neighborhood of the inner cylinder. The overall landscape of the patterns has qualitative features very similar to the SF case. In fact, when the density is computed for differ-

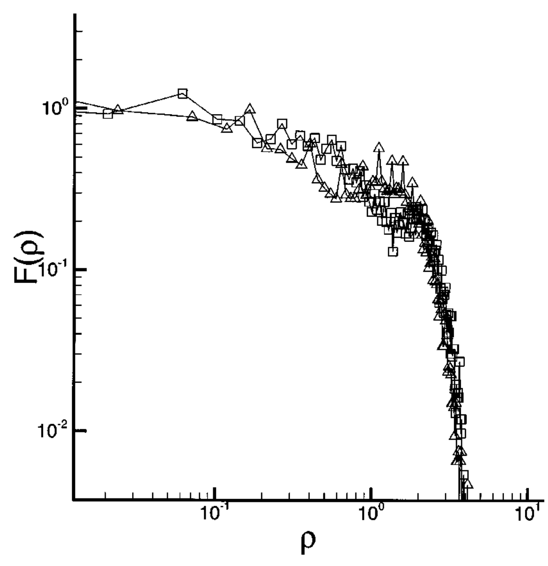

Figure 12. Probability Density Function of the box-counted density in the SF system with $T = 1.6$.

The range of density values was subdivided in $N_b = 90$ bins. Points represent the PDFs relative to $n = 3$, 4 periods. Statistics of the ICA density converges towards a time-independent distribution.

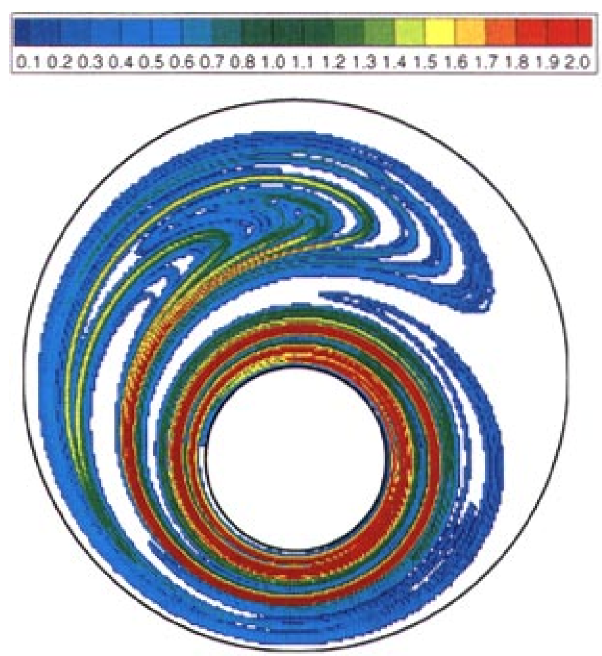

Figure 13. Box-counted ICA density from the filament depicted in Figure 9 ($\theta_{out} = 2\pi$ $n = 4$ iterations).

Flow domain was surrounded by a square of the same size as the outer diameter, and the square was subdivided in $N = 200 \times 200$ boxes. Density values below 10^{-2} are depicted as white.

ent times, it is apparent that the density is also self-similar after re-scaling (not shown).

The direct numerical tracking of interface in realistic systems is beyond the limit of current computer power, and might be altogether impossible due to exponential accumulation of unavoidable numerical errors. As a consequence, in order to characterize micromixing dynamics for flows that are relevant to industrial applications, an alternative method for estimating the density is needed. This is the object of the next two sections.

ICA Density from Local Stretching

In this section, we examine the connection between stretching and material interface dynamics to derive the ICA coarse-grained density from stretching calculations. The starting point is the concept of AD, which constitutes the theoretical framing of the qualitative observations discussed in the previous section. A detailed explanation of AD in the context of fluid mixing systems has been reported elsewhere (Muzzio et al., 2000; Giona et al., 1999; Cerbelli et al., 2000). In this article, only a brief account of the main concepts needed to understand the relationship between local and global interface dynamics is provided. AD is a specialization of the ergodic theory of dynamical systems (Oseledec, 1968; Eckmann and Ruelle, 1985). It associates an invariant geometric structure to the evolution of vectors within the chaotic region. More precisely, AD proves that at each point $\boldsymbol{x}$ of a chaotic orbit one can uniquely identify two directions $E_{\boldsymbol{x}}^u$, $E_{\boldsymbol{x}}^s$ (u stands for unstable, s for stable) characterized by the following properties:

(1) Vectors that belong to $E_{\boldsymbol{x}}^s$ are exponentially shrunk to zero norm for positive times.

(2) Vectors that belong to $E_{\boldsymbol{x}}^u$ are exponentially shrunk to zero norm for negative times (that is, under the "rewinded" mixing protocol).

In general, these directions are dependent on the point $\boldsymbol{x}$, but they are *Lagrangian-invariant*—meaning that a vector attached to the point $\boldsymbol{x}$ that belongs to either $E_{\boldsymbol{x}}^u$ or $E_{\boldsymbol{x}}^s$ is mapped through Eq. 5 into a vector that belongs to the corresponding directions at the image point. As a consequence of these properties, any vector $\delta \boldsymbol{x}$ that is attached to a chaotic initial point $\boldsymbol{X}$ rapidly collapses onto the local expanding direction while being exponentially stretched, in average, at rate Λ, where Λ is called Lyapunov exponent of the chaotic region (Figure 14). The identification of the vector $\delta \boldsymbol{X}$ with an element ds of a material line explains the invariant features exhibited by the partially mixed structures. In particular, since the filament cannot break and each piece of its arc becomes oriented exponentially fast along the local dilating direction $E_{\boldsymbol{x}}^u$, one obtains as a corollary that the entire filament structure is transformed into an invariant curve that just grows longer and longer while filling all of the space available within the chaotic region. As discussed in the previous section, this space-filling process is also invariant and nonuniform (that is, the box-counted density is time-independent and nonconstant in space). One can associate the elongation factors $\lambda^s(\boldsymbol{x})$, $\lambda^u(\boldsymbol{x})$ with the stable and unstable directions $E_{\boldsymbol{x}}^s$, $E_{\boldsymbol{x}}^u$, representing the one-step contraction-stretching of a unit vector that respectively is parallel to either of these directions. Thus, by definition, the stretching factors are just a function of position.

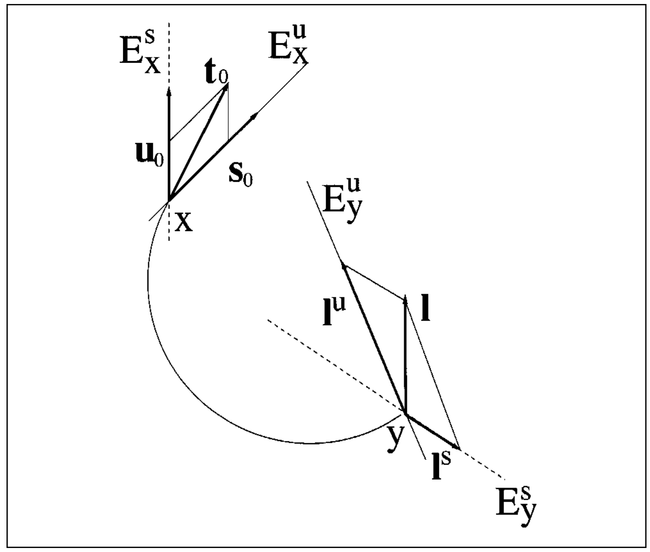

Figure 14. Invariant property of the local stable and unstable directions.

As a consequence of the fact that the component along the stable direction $\boldsymbol{s}_o$ of the initial vector $\boldsymbol{t}_o$ is shrunk exponentially fast, and the component $\boldsymbol{u}_o$ along the unstable direction is expanded exponentially, the magnitude of the image vector $\boldsymbol{l}$ increases exponentially, and the direction of $\boldsymbol{l}$ collapses onto the local expanding direction $E_{\Phi^n(x)}^u$.

Starting from the existence of this geometric template governing the geometric features of ICA, we next examine the dynamical properties of ICA density. To this end, consider a point $\boldsymbol{x} \in \mathfrak{D}_c$ with local stable and unstable directions $E_{\boldsymbol{x}}^u$ and $E_{\boldsymbol{x}}^s$ (Figure 15). With origin $\boldsymbol{x}$, we construct an infinitesimal parallelogram $P_{\boldsymbol{x}}$ ("dashed" area in Figure 15) defined by two vectors $\boldsymbol{u}$, and $\boldsymbol{s}$ laying on $E_{\boldsymbol{x}}^u$ and $E_{\boldsymbol{x}}^s$, respectively. By the invariance of the stable and unstable direction, these vectors are mapped onto the corresponding directions at the point $\boldsymbol{y} = \Phi(\boldsymbol{x})$, while their moduli are respectively multiplied by the factors $\lambda^u(\boldsymbol{x})$ and $\lambda^s(\boldsymbol{x})$. As a consequence, the parallelogram $P^{(n)}$ is mapped onto the parallelogram $P_{\boldsymbol{y}}$ at $\boldsymbol{y}$ (in the example of the figure $\lambda^u > 1$ and, therefore, lines are stretched along the unstable direction and compressed along the stable direction). Since det $(\nabla\Phi) = 1$, the two parallelograms have the same area, say δa. One can therefore use $P_{\boldsymbol{x}}$ and $P_{\boldsymbol{y}}$ as measure elements at the corresponding points. We are now able to proceed to establish a "mass" balance of ICA between the two elements at times n and $n+1$. In this balance, the properties of ICA within each element are considered constant. Also, it is assumed that stationary conditions have been reached at time n, so that the portion of filament in each measure box is composed by an array of segments parallel to the local unstable direction. Let $l^{(n)}$ denote the filament length that falls within $P_{\boldsymbol{x}}$ at the time n, $L^{(n)}$ the total filament length at the time n, $l^{(n+1)}$ the length of the portion of filament that was in $\boldsymbol{P}_{\boldsymbol{y}}$ (that is, after the application of the Poincaré map $\Phi(\boldsymbol{x})$), and $L^{(n+1)}$ the total length of the filament at time $n+1$. If the parallelograms areas are "infinitesimal," a linear approximation for ICA dynamics

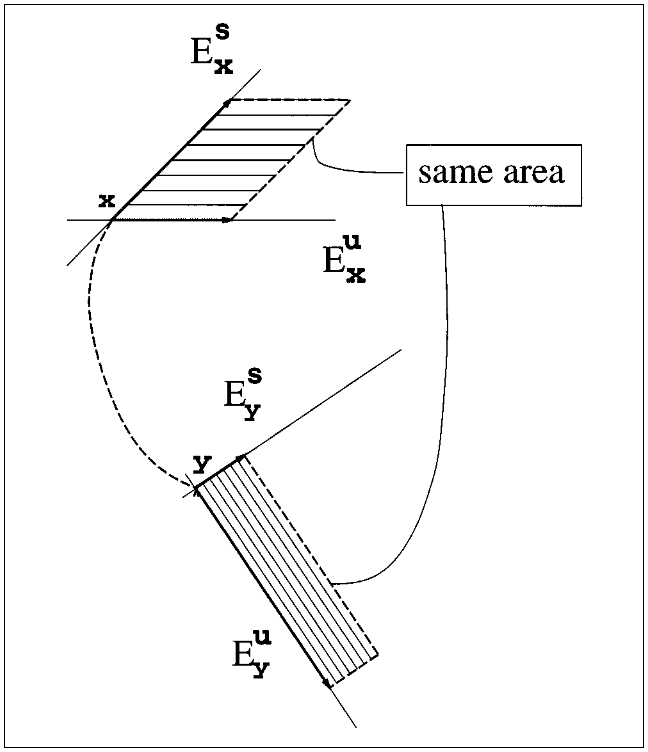

Figure 15. ICA local dynamics under the Poincaré map.

Within a linear approximation, the parallelogram P_x at x with edges parallel to the local stable and unstable directions E_x^u, E_x^s is mapped into the parallelogram P_y at $y = \Phi(x)$ with edges parallel to E_y^u and E_y^s. Since the map is area-preserving, the areas of P_x and P_y are equal. Assuming that within each parallelogram the properties of ICA are constant, and that the asymptotic orientation has been reached, it is possible to relate the densities at x and y through the elongation $\lambda^u(x)$ (Eq. 11).

holds. Therefore

$$l^{(n+1)} = \lambda^u(\boldsymbol{x}) l^{(n)} \tag{10}$$

Since $\rho_n(\boldsymbol{x})$ is normalized by the total filament length, we set $\rho_n(\boldsymbol{x}) = l^{(n)}/L^{(n)}$, and $\rho_{n+1}(\boldsymbol{y}) = l^{(n+1)}/L^{(n+1)}$. By using these definitions one can recast Eq. 10 into

$$\rho_{n+1}(\Phi(\boldsymbol{x})) = \frac{L^{(n)}}{L^{(n+1)}} \rho_n(\boldsymbol{x}) \lambda^u(\boldsymbol{x}) \tag{11}$$

Equation 11 generates, by recursion, a sequence of functions $\rho^{(n)}(\boldsymbol{x})$. By taking the limit of Eq. 11 as n goes to infinity, one obtains formally that the pointwise stationary density $\rho(\boldsymbol{x})$ that builds up the coarse-grained average $\rho(\boldsymbol{x}_i)$ observed by direct interface tracking must satisfy the relationship

$$\rho_\infty(\Phi(\boldsymbol{x})) = \frac{\rho_\infty(\boldsymbol{x}) \lambda^u(\boldsymbol{x})}{e^\nu} \tag{12}$$

where the exponential of the topological entropy provides the limit value of $L^{(n+1)}/L^{(n)}$. Since $\rho(\boldsymbol{x})$ is a probability measure (that is, its integral over the chaotic region is equal to unity), the exponent ν must satisfy the relation

$$e^\nu = \int \rho(\boldsymbol{x}) \lambda^u(\boldsymbol{x}) d\boldsymbol{x} \tag{13}$$

From the theoretical standpoint, the foremost problem in defining $\rho_\infty(\boldsymbol{x})$ as the limit of the sequence given in Eq. 11 is to determine whether this limit exists, and, in case it does exist, to establish what are the smoothness characteristics of the limit function. Indeed, even under the assumption that the elongation $\lambda^u(\boldsymbol{x})$, (therefore, any function of the sequence) is smooth, the limit of the sequence does not need to retain this feature. These fundamental questions, which are beyond the scope of this article, will be addressed elsewhere. Here, we exploit the structural form of Eq. 11 to define the properties of the coarse-averaged density. First, one observes that, by denoting with $\boldsymbol{x}_{-i} = \Phi^{-i}(\boldsymbol{x})$, Eq. 11 can be rewritten as

$$\rho_n(\boldsymbol{x}) = \rho_0(\boldsymbol{x}_{-n}) \frac{\prod_{i=-n}^{i=-1} \lambda^u(\boldsymbol{x}_{-i})}{e^{n\nu}} = \rho_0(\boldsymbol{x}_{-n}) \frac{\lambda_n^u(\boldsymbol{x}_{-n})}{e^{n\nu}} \tag{14}$$

In other words, one can hold the current position $\boldsymbol{x}$ fixed, and consider the backward density generation process. Also, by considering that the evolved interface structure is independent of the initial condition, one can start with a uniform distribution of ICA for which $\rho^{(0)} \equiv 1$, hence, obtaining an explicit relationship for the density $\rho^{(n)}(\boldsymbol{x})$.

In order to obtain the box-averaged density, we subdivide the flow domain in N_b cells centered at the points $\boldsymbol{x}_i$, and cover the domain with a uniformly distributed array of N_p points. The number $N_p \gg N_b$ is chosen in such a way that the average number of points per cell is large enough to determine accurate statistics within each cell. The box-averaged density $\langle \rho_\lambda^{(n)} \rangle_{\boldsymbol{x}_i}$ as predicted by the stretching average then reads

$$\langle \rho_\lambda^{(n)} \rangle_{\boldsymbol{x}_i} = \frac{\sum_{\mathcal{B}_i} \lambda_n^u(\boldsymbol{x}_{-n})}{e^{n\nu}} \tag{15}$$

where the sum is taken over the ensemble $\mathcal{B}_i$ representing the n-th preimages of all the points that currently fall within the box centered at $\boldsymbol{x}_i$. In order to simplify the notation the box-averaged n-th order stretching at $\boldsymbol{x}_i$ is hereafter denoted by

$$\lambda_{n,c}(\boldsymbol{x}_i) = \sum_{\mathcal{B}_i} \lambda_n^u(\boldsymbol{x}_{-n}) \tag{16}$$

Notice that the normalization condition on the coarse-averaged density requires that

$$\sum_{i=1}^{i=N_b} \lambda_{n,c}(\boldsymbol{x}_i) = \langle \lambda_{n,c} \rangle = \sum_{j=1}^{j=N_p} \lambda_n^u(\boldsymbol{x}_{-n}) = e^{n\nu} = \int \lambda^u(\boldsymbol{x}) d\boldsymbol{x} \tag{17}$$

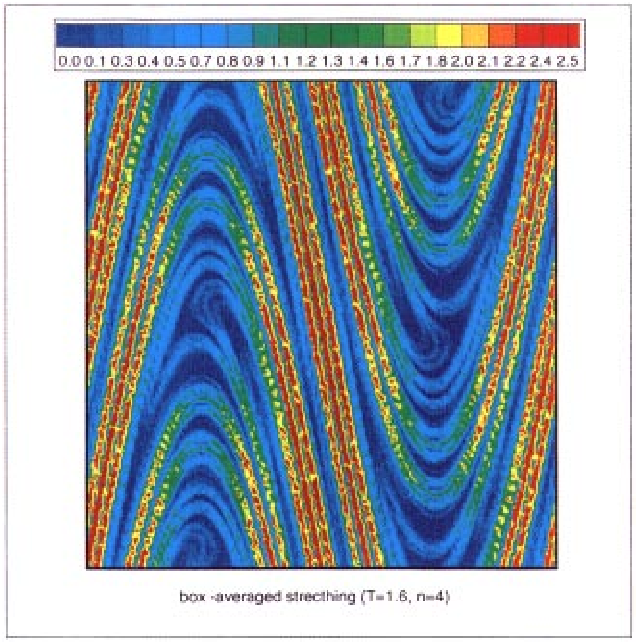

Figure 16. Density of ICA from coarse stretching average.

The unit box was subdivided in $N_b = 150 \times 150$ boxes, and the normalized coarse stretching $\langle \rho_\lambda^{(n)} \rangle_{x_i}$ was computed for $n = 4$ periods. The contour levels were chosen identical to those of Figure 12. The quantitative agreement between the two computations proves that the relationship between ICA density and stretching is verified for a finite size box covering of the flow domain.

From a practical point of view, in order to compute the box-averaged density through the stretching average defined by Eq. 16, there is no need to consider the inverse Poincaré map $\Phi^{-1}(\boldsymbol{x})$. Indeed, one can start from a uniform distribution of points together with the attached unit tangent vectors and map them forward for n periods. The density $\langle \rho_\lambda^{(n)} \rangle_{x_i}$ can be then calculated by associating to each box i the n-th order stretching $\lambda_{n,c}$ obtained as the average of all the stretching values associated with points that fall within the box *at the final time*.

Results of this computation for the SF system are shown in Figure 16 in the nearly globally chaotic case $T = 1.6$. In this case, $N_p \approx 4 \times 10^6$ points were mapped for four periods, and the coarse stretching statistics was determined by subdividing the unit square into $N_b = 150 \times 150$ boxes. The figure reports the color-coded contour plot, together with the legend for each color range. The contour levels are chosen to be identical to those of Figure 11 where the filament density was evaluated by direct numerical simulation of the interface. The comparison between Figure 16 and Figure 11 shows that a qualitative and quantitative agreement between the two computations holds, thus proving that the relationship between stretching and density given in Eq. 11 is verified. The agreement is also perfect in the statistical domain, as it is shown in Figure 12 where the PDF of the values ρ_λ is represented by the triangles.

As previously discussed, the importance of being able to compute densities from stretching can hardly be overestimated in situations where the velocity field is not known analytically. This is the case, for instance, of all of the industrially relevant 3-D flows, where the determination of the flow field relies on computational fluid dynamics (CFD) techniques. In the next section, a generalization of the concepts developed in the context of 2-D time-periodic flows to generic time-dependent chaotic flows is presented.

Interface Dynamics in Aperiodic Flows

The study of time periodic systems showed that, depending on the value of the period, different phase space landscapes are possible, going from a nearly integrable picture (where the chaotic region is confined to a small portion of the flow domain), to a condition of almost global chaos. Since the main goal, from the macromixing optimization viewpoint, is to destroy segregated regions, the search for protocols that fall within "mixing windows" has received special attention in the laminar mixing literature (Ling, 1993; Ling and Schmidt, 1992). Unfortunately, the sampling within the parameter space to determine the global chaos condition must be addressed on a case-by-case basis, since no general technique for predicting the phase space structure corresponding to a given parameter value is available at the present time.

Recent work has focused on the alternative route of relaxing the periodicity constraint and studing the optimization problem within the general framework of 2-D time-dependent flows (Franjione and Ottino, 1992; Liu and Muzzio, 1994); Poje et al., 1999). This idea is motivated by the observation that segregated regions are associated with periodic elliptic points and therefore, *mixing recipes devoid of periodicity are also devoid of islands*. In addition, we hypothesize that a better understanding of the properties of aperiodic chaotic flows can help understand mixing in turbulent flows, where the aperiodic "random" perturbation is a (zero-mean) time-dependent field superimposed to the mean (that is, time-averaged) flow field.

In spite of its considerable theoretical and practical interest, the characterization of mixing in aperiodic flows still lacks a homogeneous formal framing that is able to capture the essential features of mixing dynamics for different flow recipes. The first problem is that the discretization of the dynamics via the stroboscopic map does not yield an autonomous (that is, time-independent) system. Indeed, if one takes snapshots at regular intervals of time, say τ, the evolution of each point of the flow domain is given by

$$\boldsymbol{x}_{n+1} = \boldsymbol{\Phi}_\tau^{(n)}(\boldsymbol{x}_n) \tag{18}$$

where the superscript (n) indicates that the stroboscopic map depends explicitly on the discretized time $n = t/\tau$. Therefore the dynamics is specified by *a sequence* of transformations, rather than the repeated application of single map (recent advances extending the results of Oseledec's theorem to this case can be found in Liu and Qian, 1995). In this situation, intuition suggests that one should not expect to find time-invariant properties. Nevertheless, focusing on the dynamics on the tangent space (that is, on the orientation of tangent vectors), reveals that a generalized form of asymptotic directionality still holds. In this context, AD is the property by which the tangent vectors dynamics loses its dependence on the initial orientation to yield a field of (unstable) orientations that

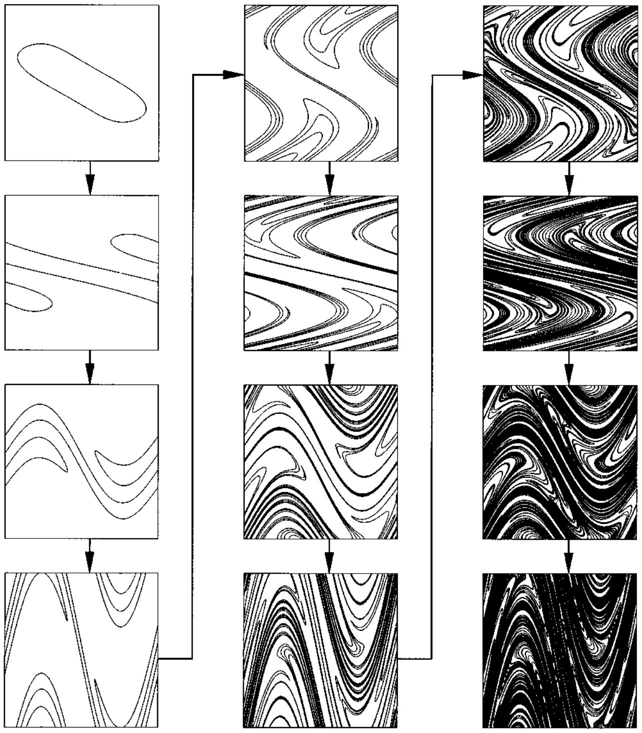

Figure 17. Evolution of ICA in the periodic SF system ($T = 1.6$).

Four snapshots per period are taken for the first three periods. Frames are arranged in a tabular array, where each column represents the dynamics within each period (left column $n = 1$, center column $n = 2$, right column $n = 3$). Time increases from top to bottom and left to right as indicated by the arrows.

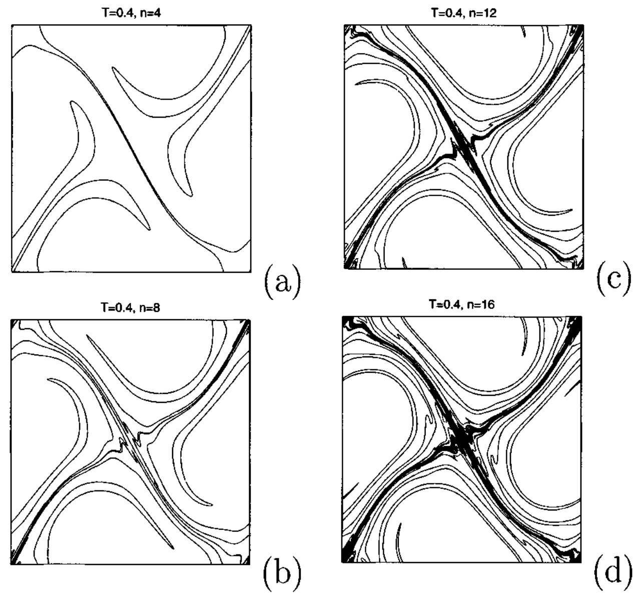

Figure 18. ICA dynamics in the SF system with $T = 0.4$.

is a function of time only. In order to understand this fading memory property, a closer re-examination of the links between the time-continuous evolution and its discretized form is necessary. The periodic case can serve as a conceptual bridge between the two frames. To this end, consider a time periodic flow of period T, and construct a finer discretization of the time variable by taking snapshots of the dynamics at intervals $\tau = T/h$, where $h > 1$ is an integer. In this case, we have a set of h distinct time-τ maps $\mathbf{\Phi}_\tau^{(i)}(\boldsymbol{x})$, $i = \{1, 2, \ldots, h\}$, none of which coincides with the Poincaré map, since we are taking intervals of time that are different than the period of the flow field. Nevertheless, for the periodic case, the relationship between the time-τ maps and the Poincaré map $\mathbf{\Phi}(\boldsymbol{x})$ is easy to obtain

$$\mathbf{\Phi}(\boldsymbol{x}) = \underbrace{\mathbf{\Phi}_\tau^{(h)} \circ \mathbf{\Phi}_\tau^{(h-1)} \circ \cdots \mathbf{\Phi}_\tau^{(1)}}_{h \text{ factors}} \tag{19}$$

where $\circ$ denotes composition.

Figure 17 shows the stroboscopic evolution of ICA in the SF system ($T = 1.6$) for a time $\tau_{\max} = 3T$, snapshots taken at intervals $\tau = T/6$. The frames are arranged in a tabular array of three columns, where each column covers one complete period. Therefore, frames that lay on the same row represent states of the filament at integer multiples of the period T. While the convergence towards a time-invariant shape is evident for any row, the difference between the invariant structures in different rows indicates that in the time continuous evolution, the field of dilating directions is time-periodic with the same period T of the flow field. By a straightforward generalization, one expects that for an aperiodic chaotic flow, the fields of dilating and contracting directions are time-dependent and particularly aperiodic. Yet, the statistical properties of ICA settle onto a time-invariant behavior. Figures 18 and 19 show four snapshots of the same initial condition

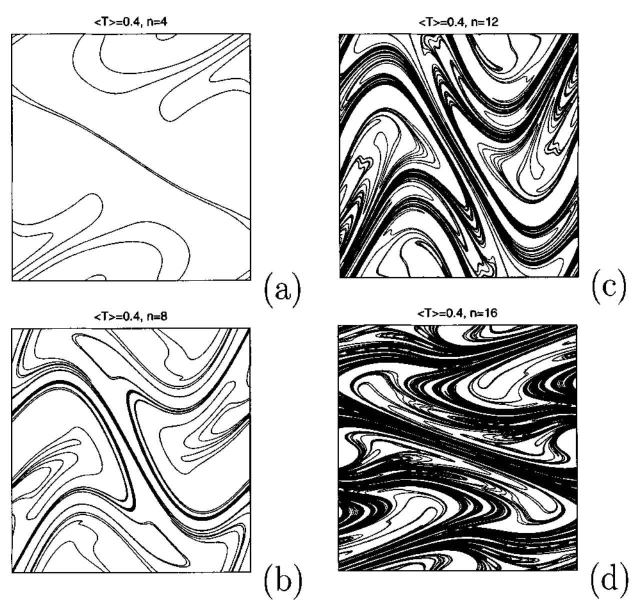

Figure 19. ICA dynamics in the SF system for the aperiodic recipe $\langle T \rangle = 0.4$; $\alpha = 1$.

Comparison with corresponding (unperturbed) periodic case (Figure 18) shows that the generation of ICA is dramatically enhanced by the periodicity breakup in those regions that are segregated islands for the periodic protocol.

used throughout the previous section for a periodic ($\alpha = 0$) and an aperiodic recipe ($\alpha = 1$) about the nominal period $\langle T \rangle = 0.4$. The dimensionless times $\tau = 1, 2, 3, 4$ correspond in this case to $n = 4, 8, 12, 16$ nominal periods. The comparison highlights the following points for aperiodic flows:

(1) The mixing patterns are indeed time-dependent.

(2) The distribution of ICA throughout the flow domain is still nonuniform, with a high density region located about the hyperbolic fixed point $\boldsymbol{x} = (1/2, 1/2)$. Note that this point is still a fixed point for the stroboscopic map, even in the aperiodic recipe.

(3) The process of generation of ICA is enormously enhanced within the region that corresponds to the islands in the periodic case.

A global quantitative measure of the improvement in the process of generation of ICA is represented in Figure 20 (square symbols), which shows the growth of ICA vs. time. The comparison with Figure 10 shows that the overall length of the material line at the final time $\tau = 4$ undergoes almost a ten-fold increase with respect to the base periodic case. The triangle and circle symbols in the figure represent the ICA growth for perturbations (with the same strength $\alpha = 1$) about the nominal period $\langle T \rangle = 0.80$, and $\langle T \rangle = 1.6$, respectively (the corresponding snapshots displaying the geometric structure of the filament are not shown in the interest of brevity). The comparison between the overall ICA growth for the periodic (Figure 10) and aperiodic recipes (Figure 20) indicates that the rate of growth becomes independent of the perturbation as the base periodic case becomes closer to being nearly globally chaotic. In other words, from the above results we surmise that the topological entropy of a 2-D time-dependent chaotic flow is a characteristic of the geometry of the system and of the two blinking steady fields $\boldsymbol{v}_1$, $\boldsymbol{v}_2$, but not of the parameter T.

This suggests the dynamical properties of time-dependent flows are generically associated with the presence of chaos (for example, in the aperiodic case with the exponential divergence of length for almost all the points of the flow domain), independent of whether the chaotic behavior is reached through a periodic or an aperiodic protocol.

However, these observations are derived from the results of a particular class of aperiodic flows, and it would be unwise to jump to general conclusions. As a matter of fact, the realm of aperiodic flows is so wide than it is not even clear what questions one should ask.

An important point arises as to whether the convergence towards a stationary process is characteristic of overall measures of chaos (such as the topological entropy), or if it can also be observed in local properties. As a matter of fact, global parameters are not enough to describe the dynamics when convective mixing is associated with nonlinear phenomena occurring in the bulk of the fluid; witness the wide spatial varaition of $\rho(\boldsymbol{x})$.

This point is investigated next through the coarse-grained density, $\rho_n(\boldsymbol{x}_i)$ as defined in the Introduction, and the box-averaged stretching $\lambda_{n,c}(\boldsymbol{x}_i)$ as defined in Eq. 16. As a matter of fact, neither stretching nor the ICA density computations require the flow to be time-periodic. Furthermore, the relationship between stretching and density, given by Eq. 11, is only based on the hypothesis that the AD property (in the broad meaning of fading memory with respect to initial orientation) holds. To confirm this hypothesis, Figure 21 shows the comparison between the spatial fields $\langle \rho^{(n)} \rangle_{\boldsymbol{x}_i}$ and $\langle \rho_\lambda^{(n)} \rangle_{\boldsymbol{x}_i}$ for the protocol $\langle T \rangle = 0.8$, $\alpha = 1$ after $n = 11$ nominal periods. As customary, the same scale for the color con-

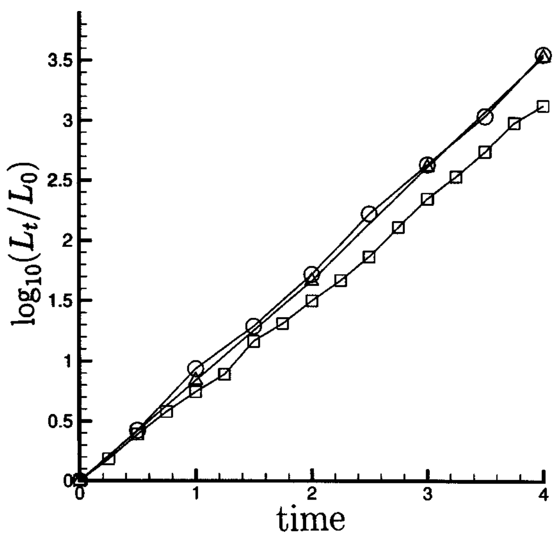

Figure 20. Overall growth of ICA in the aperiodic SF system.

∘: $\langle T \rangle = 1.6$, Δ: $\langle T \rangle = 0.8$; (□): $\langle T \rangle = 0.4$. The strength of perturbation α is set to unity in all of the cases considered.

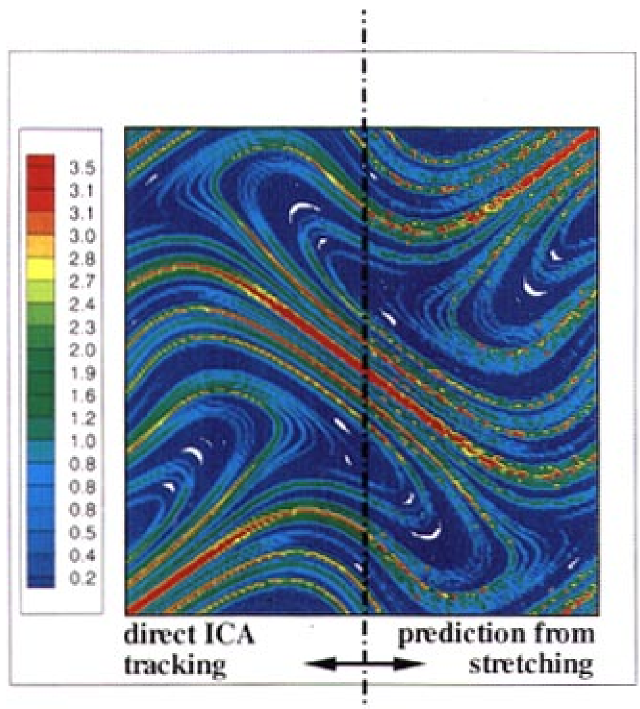

Figure 21. Coarse-grained statistics in the aperiodic SF system.

Comparison between the box-counted density obtained through ICA tracking and the prediction obtained through box-averaged stretching. The case shown is $\langle T \rangle = 0.8$, $\alpha = 1$.

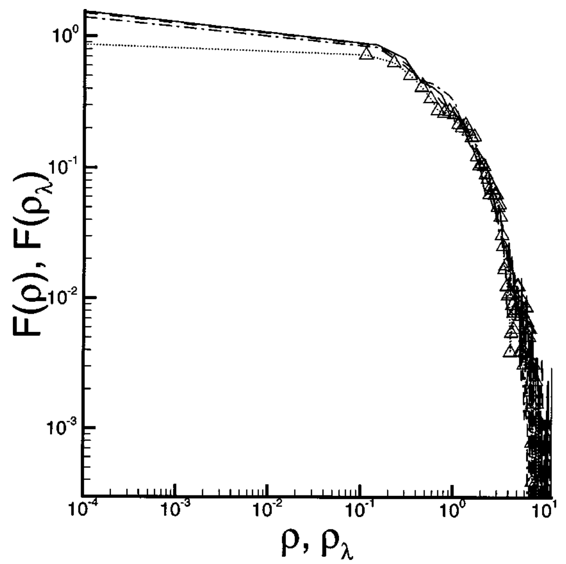

Figure 22. PDF of the box-counted filament density for the aperiodic SF system.

($\langle T \rangle = 0.8$; $\alpha = 1$ for ($\square$) $n = 10$, and (Δ) $n = 12$ nominal periods.

tour plot was used in both cases. As before, both results are essentially identical, confirming that Eq. 11 provides a feasible method for computing ρ in any type of mixing flow.

A subtler point is to establish the meaning of time-invariant behavior in the aperiodic context. Indeed, from the structures of ICA at different times, it is clear that one cannot expect either the coarse-grained density or the box-averaged stretching spatial patterns to be time-invariant. However, both dynamics settle onto a *stationary* process characterized by time-invariant statistics. Figure 22 shows the PDF's of $F(\langle \rho^{(n)} \rangle_{x_i})$ at three different times (continuous, dashed and dash-dotted lines corresponding to $n = 9$, 10, 11 multiples of the nominal periods, respectively). The dotted lines connecting the triangles represent the PDF $F(\langle \rho_\lambda^{(n)} \rangle_{x_i})$ at time $n = 11$. The time independence of each distribution, as well as the equivalence of stretching and density statistics, implies that these properties are generic within the class of flows considered in this article.

In summary, for a generic time-dependent flow, the concept of time invariance characteristic of time-periodic flows generalizes into the concept of *stationary* process. This means that once the "steady state" (that is, the independence from the initial orientation) has been reached, the patterns of the coarse-grained density (or, equivalently the box-averaged stretching) change with time, but the statistics of the values is preserved. Loosely speaking, one can envision this property as a process where "mixing cells" dynamically exchange values with each other on a one-to-one basis, so that the frequency of each value remains unchanged.

Conclusions

Quantitative methods able to capture the geometric and dynamic features of the ICA in partially-mixed structures in chaotic laminar flows were presented in this article. The study of ICA dynamics was first analyzed in the context of time-periodic flows through the following steps:

(1) The density of ICA was defined as a box-counted concentration of filament length. The computation of density required to develop an efficient tracking algorithm able to preserve the continuity of the interface, while it evolved towards a highly convoluted structure of exponentially increasing length. Computations of ICA dynamics demonstrate that this structure is characterized by a nonuniform stationary (that is, statistically time-independent) density for all the (periodic and aperiodic) chaotic flows considered. Even for simplified 2-D flows, such as the ones considered in this article, this analysis is at the limit of the current computational power.

(2) The link between the global dynamics of ICA and the standard local analysis (that is, the stretching of an infinitesimal element of line) was found by further developing some general results of ergodic theory. The specialization of these results for fluid mixing systems lead to the concept of AD, which provides the key to explaining the invariant features of partially mixed structures within the chaotic region. In particular, the AD property allowed us to derive the relationships between ICA density and stretching dynamics. The importance of this relationship is fundamental, since the coarse-grained analysis of stretching is robust to numerical investigation and can be potentially performed in any flow.

The structural relationship between stretching and interface density was then generalized to the case of a time-dependent (but not necessarily periodic) chaotic flow. The comparison between ICA density as predicted by box-counted particle stretching, and as computed through direct numerical tracking, showed a quantitative agreement. The theoretical counterpart of this finding is the generalization of the AD property to the case of aperiodic flows, which in the time-discrete setting is represented by an aperiodic sequence of mappings. In this broader context, AD is the property by which line elements possess exponentially fading memory of their initial orientation as time goes by. This property causes the mixing structures to converge towards a pattern that is independent of the location and shape of the originally segregated region.

As expected, the spatial organization of ICA inherits the same time-dependent features of the mixing protocol by which it is generated. However, the statistical properties of ICA density settle onto time-independent behavior depending upon the mixing recipe adopted. In other words, Lagrangian transport of passive interfaces in chaotic flows can be modeled as an Eulerian stationary process in which a number of elementary cells, representing the spatial modulation of the stretching, dynamically exchange ICA while preserving statistical invariance.

Acknowledgment

FJM wishes to thank Dow Chemical Company for supporting this work.

Literature Cited

Alvarez, M. M., F. J. Muzzio, S. Cerbelli, A. Adrover, and M. Giona, "Self-Similar Spatiotemporal Structure of Intermaterial Boundaries in Chaotic Flows", *Phys. Rev. Lett.*, **81**, 3395 (1998).
Aref, H., "Stirring by Chaotic Advection," *J. Fluid Mech.*, **143** 1 (1984).

Cerbelli, S., J. Zalc, and F. J. Muzzio,"The Evolution of Material Lines Curvature in Deterministic Chaotic Flows," *Chem. Eng. Sci.*, **55**, 1497 (2000).
Eckmann, J.-P., and D. Ruelle, "Ergodic Theory of Chaos and Strange Attractors," *Rev. Modern Phys.*, **57**, 617 (1985).
Fountain, G. O., D. V. Khakhar, and J. M. Ottino, "Visualization of Three-Dimensional Chaos," *Science*, **281**, 683 (1998).
Franjione, J. G., and J. M. Ottino, "Symmetry Concepts for the Geometric Analysis of Mixing Flows," *Phil. Trans. R. Soc. Lond. A*, **338**, 301 (1992).
Giona, M., A. Adrover, F. J. Muzzio, S. Cerbelli, and M. M. Alvarez, "The Geometry of Mixing in Time-Periodic Chaotic Flows: I. Asymptotic Directionality in Physically Realizable Flows and Global Invariant Properties," *Phys. D*, **132**, 298 (1999).
Hobbs, D. M., M. M. Alvarez, and F. J. Muzzio, "Mixing in Globally Chaotic Flows: A Self-Similar Process," *Fractals*, **5**, 395 (1997).
Katok, A., and B. Hasselblatt, "Introduction to the Modern Theory of Dynamical Systems," Cambridge University Press, Cambridge (1995).
Ling, F. H., "The Effect of Mixing Protocol on Mixing in Discontinuous Cavity Flows," *Phys. Lett. A*, **117**, 331 (1993).
Ling, F. H., and G. Schmidt, "Mixing Windows in Discontinuous Cavity Flows," *Phys. Lett. A*, **165**, 221 (1992).
Liu, M., and F. J. Muzzio, "Quantification of Mixing in Aperiodic Chaotic Flows," *Chaos, Solitons and Fractals*, **4**, 869 (1994).
Liu, Pei-Dong, and Min Qian, "Smooth Ergodic Theory of Random Dynamical Systems," Springer-Verlag, Berlin, 1995.
Muzzio, F. J., S., Alvarez, M. M. Cerbelli, M. Giona, and A. Adrover, "The Intermaterial Area Density Generated by Time- and Spatially Periodic 2d Chaotic Flows," *Chem. Eng. Sci.*, **55**, 363 (2000).
Muzzio, F. J., and J. M. Ottino, "Evolution of a Lamellar System with Diffusion and Reaction: A Scaling Approach," *Phys. Rev. Lett.*, **63**, 47 (1989).
Newhouse, S. E., "Entropy and Volume as Measures of Orbit Complexity," *The Physics of Phase Space* (College Park, Md., 1986), (Also published by Springer, Berlin (1987)).
Oseledec, V. I., "A Multiplicative Ergodic Theorem. Characteristic Ljapunov, Exponents of Dynamical Systems," *Trudy Moskov. Mat. Obšč.*, **19**, 179 (1968).
Ottino, J. M., "The Kinematics of Mixing: Stretching, Chaos, and Transport," Cambridge University Press, Cambridge (1989).
Poje, A. C., G. Haller, and I. Mezić, "The Geometry and Statistics of Mixing in Aperiodic Flows," *Phys. Fluids*, **11**, 2963 (1999).
Sokolov, I. M., and A. Blumen, "Bimolecular Reactions Between Passively Transported Species," *Phys. Lett. A*, **178**, 364 (1993).
Wannier, G. H., "A Contribution to the Hydrodynamics of Lubrication," *Quart. Appl. Math.*, **3**, 1 (1950).

Manuscript received May 22, 2000, and revision received Dec. 7, 2000.